Int. J. Heat Mass Transfer. Vol. 36, No. 3, pp. 651–662, 1993
Printed in Great Britain

0017-9310/93 $6.00+0.00

Vapor bubble departure in forced convection boiling

J. F. KLAUSNER,† R. MEI,‡ D. M. BERNHARD† and L. Z. ZENG†

† Department of Mechanical Engineering, University of Florida, Gainesville, FL 32611, U.S.A.
‡ Department of Aerospace Engineering, Mechanics and Engineering Science, University of Florida, Gainesville, FL 32611, U.S.A.

(*Received* 29 *October* 1991 *and in final form* 9 *March* 1992)

Abstract—A forced convection boiling facility has been fabricated in which vapor bubble departure can be investigated. It has been observed that once a vapor bubble departs from its nucleation site, it typically slides along the heating surface and lifts off at some finite distance downstream. The probability density functions (pdfs) for bubble departure diameter, d, have been obtained for mass flux, G, ranging from 112 to 287 kg m^{-2} s^{-1} and heat flux, q_w, ranging from 11.0 to 26.0 kW m^{-2}. The data indicate a systematic dependence of d on G and q_w. A detailed analysis of various forces acting on the bubble is presented and is used to predict the mean departure diameter. The onset of imbalance between the quasi-steady drag, the unsteady component of the drag due to asymmetrical bubble growth, and the surface tension force in the flow direction is used as a criterion for departure and yields satisfactory agreement between the measured and predicted values of the mean departure diameter. The analytical prediction shows a strong influence of mean liquid velocity and wall superheat on the bubble departure diameter. At the point of departure the surface tension force in the flow direction is generally small.

1. INTRODUCTION

In order to obtain a mechanistic model for the microconvective component of heat transfer in flow boiling, detailed information on the nucleation, growth, departure, and lift-off of vapor bubbles is required. An experimental facility has been fabricated in which a saturated two-phase mixture of refrigerant R113 flows through a 25 × 25 mm square visual boiling section. It has been observed that once a vapor bubble departs from a nucleation site, it typically slides along the heating surface and continues to grow until it lifts off from the surface at some finite distance downstream of the nucleation site. In this work the instant a vapor bubble leaves the nucleation site is taken to be the departure point, while the instant a vapor bubble lifts off the heating surface is referred to as the lift-off point. A distinction between the departure and lift-off point is necessary since a vapor bubble contributes to the microconvective heat transfer process as long as it remains attached to the heating surface. At times it has been observed that the vapor bubble directly lifts off the heating surface without first sliding. The frequency of this occurrence is insignificant for the range of flow conditions examined. In this work, vapor bubble departure in saturated forced convection boiling is investigated. Vapor bubble lift-off will be covered in a subsequent study.

Although there have been a large number of studies investigating vapor bubble departure in pool boiling, few similar studies have been carried out for flow boiling. Chang [1] developed an expression for flow boiling departure diameter by assuming the instant a vapor bubble departs the heating surface is the point where the net forces acting on a vapor bubble (including forces acting parallel and normal to the heating surface) just balance each other. Sliding bubbles were not considered, and the expression was never experimentally verified. Hsu and Graham [2] conducted a visual study for upflow boiling of water in various flow regimes. Vapor bubble departure was observed for bubbly flow. Although it was not stated in the text, it appears from their diagram of bubble trajectory that vapor bubbles slide along the heating surface before lifting off. Levy [3] obtained a vapor bubble departure diameter correlation for upflow subcooled boiling of water. The instant a vapor bubble departed a heated wall was taken to be the point at which the net forces in the flow direction acting on the growing vapor bubble just balanced each other. A wide range of flow conditions was considered, and it was found that at a mass flux, G, as low as 135 kg m^{-2} s^{-1} in a 37.7 mm i.d. tube the buoyancy force acting on a vapor bubble was of negligible influence compared with the drag force. No mention was made if the vapor bubbles slide along the heating surface before lifting away. Koumoutsos *et al.* [4] studied vapor bubble lift-off from an artificial nucleation site with saturated water flowing horizontally through a 15 × 26 mm rectangular channel with mass flux, G, ranging from 38 to 356 kg m^{-2} s^{-1}. They also observed that soon after incipience vapor bubbles begin to slide away from the nucleation sites and continue to grow until they lift off the surface. They obtained a correlation for lift-off diameter based on a vapor bubble net force balance (including forces acting both parallel and normal to the flow direction). The buoyancy force was found to be of significant influence. Cooper *et al.* [5] have stud-

NOMENCLATURE

a	vapor bubble radius [m or mm]
c_p	specific heat [J kg^{-1} °C^{-1}]
d	vapor bubble departure diameter [m or mm]
d_w	surface/bubble contact diameter [m]
D	square channel inner width [m or mm]
F	force [N]
G	mass flux [kg m^{-2} s^{-1}]
h_{fg}	latent heat of vaporization [J kg^{-1}]
q_w	heat flux [kW m^{-2}]
T_{sat}	saturation temperature [°C or K]
ΔT_{sat}	wall superheat [°C]
t	time [s]
u	area average velocity [m s^{-1}]
$U(y)$	liquid velocity profile near wall [m s^{-1}]
u^*	friction velocity [m s^{-1}]
X	vapor quality.

Greek symbols

α	advancing contact angle
β	receding contact angle
γ	circumferential contact angle
δ	liquid film thickness [m or mm]
θ_i	inclination angle
ν	kinematic viscosity [m^2 s^{-1}]
ρ	density [kg m^{-3}]
σ	surface tension [N m^{-1}].

Subscripts

l	liquid
v	vapor
x	x-direction
y	y-direction.

ied the growth and departure of vapor bubbles with laminar upflow of saturated n-hexane over a flat plate. They reported that vapor bubbles roll along the heating surface and for this reason they claim that the point of departure is not well defined. Furthermore, they mentioned that the simple force balances used by Levy [3] and Koumoutsos *et al.* [4] were insufficient for modelling their vapor bubble departure data. It is apparent that the force balance analyses of Chang [1], Levy [3], and Koumoutsos *et al.* [4] neglect the difference between the advancing and receding surface to bubble contact angles when modelling the surface tension force. Their attempts to account for this difference with a proportionality constant are not fundamentally sound.

In this study probability density functions (pdfs) for vapor bubble departure over a range of flow conditions are experimentally obtained. The strong dependence of the mean departure diameter on the mass flux highlights the importance of the quasi-steady drag force, while the influence of the heat flux on the mean departure diameter highlights the importance of the unsteady drag force due to asymmetrical bubble growth. Furthermore, the significant standard deviation of the departure diameters from the mean is indicative of the stochastic nature of the bubble departure process. Guided by the experimental findings, a detailed analysis of various forces on the bubble in the directions parallel and normal to the heating surface is developed and used to describe both quantitatively and qualitatively the physics governing the departure process. The forces acting on the bubble include the surface tension force, the quasi-steady drag, the unsteady drag due to asymmetrical bubble growth, the shear lift force, the buoyancy force, the hydrodynamic pressure force, and the contact pressure force. For the flow conditions experimentally investigated, the analysis predicts that the bubbles will slide prior to lifting off. The predicted mean departure diameter based on the analysis is in satisfactory agreement with measured values. The dependence of the mean departure diameter on the mean liquid velocity and wall superheat is elucidated.

2. EXPERIMENTAL FACILITY

An experimental forced convection boiling facility using refrigerant R113 designed for flow visualization has been fabricated. A schematic diagram of the flow boiling facility is displayed in Fig. 1. A variable speed model 221 Micropump is used to pump R113 through the facility. The volumetric flow rate of refrigerant through the facility is monitored with an Erdco Model 2521 vane type flow meter equipped with a 4-20 ma analog output. Calibration of the flow meter demonstrates that it is accurate to within ±0.5% of full scale, which is the repeatability claimed by the manufacturer. At the outlet of the flow meter five preheaters with a maximum heat rate of 5 kW have been installed. Each preheater consists of a 25.4 mm i.d., 1.2 m long hard copper pipe around which 18 gauge nichrome wire has been circumferentially wrapped. The nichrome wire is electrically insulated from the copper pipe with ceramic beads. The heaters are thermally insulated with 25.4 mm thick fiberglass insulation. The voltage inputs to the preheaters are controlled with five 240 V a.c. autotransformers. The heat loss from the preheaters as a function of temperature difference between the insulation outer surface and ambient has been predetermined from calibration.

The horizontal flow boiling visual test section is located downstream of the preheaters. A capacitance based liquid film thickness sensor, described in detail by Klausner *et al.* [6], has been installed on either side

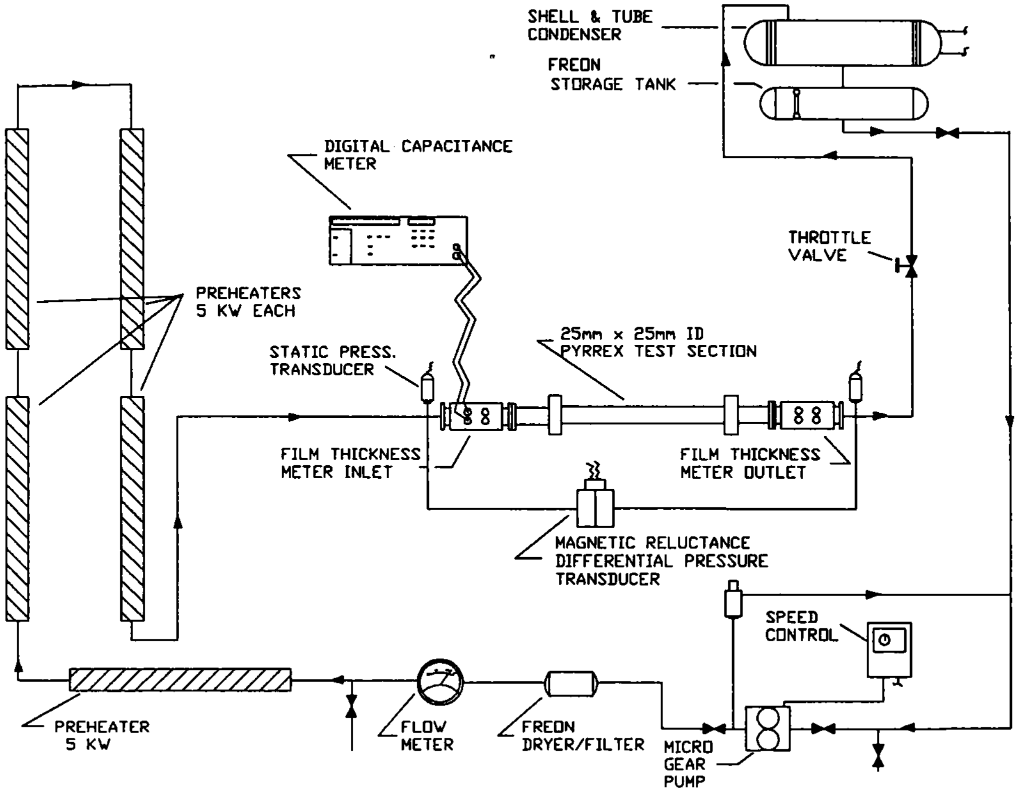

FIG. 1. Schematic diagram of flow boiling facility.

of the test section. An isometric view of the test section is displayed in Fig. 2. The main body is comprised of a 25 × 25 mm inner width square pyrex tube that is 4 mm thick and 0.457 m long. A 0.13 mm thick and 22 mm wide nichrome strip, used for heating, has been adhered to the lower surface of the square tube with epoxy. Six equally spaced 36 gauge type E thermocouples have been adhered to the back side of the nichrome strip using high thermal conductivity epoxy. A heat conduction analysis indicated that there exists essentially no temperature difference between the front and back side of the strip for the range of heat fluxes encountered in this investigation. The test section is connected to the facility with garolite compression flanges. The garolite flanges have been adhered to the ends of the pyrex tube with epoxy. The flanges have been compressed between a brass block and a copper plate. The ends of the heating strip were bent 180° around the ends of the pyrex tube, and the flanges were fitted over the heating strip. Each end of the heating strip is compressed between the copper plate and the garolite flange. Since the copper plate makes electrical contact with the brass block, the nichrome heating strip is also in electrical contact with the block. In order to heat the strip, a 36 V, 120 A d.c. power supply has been electrically connected

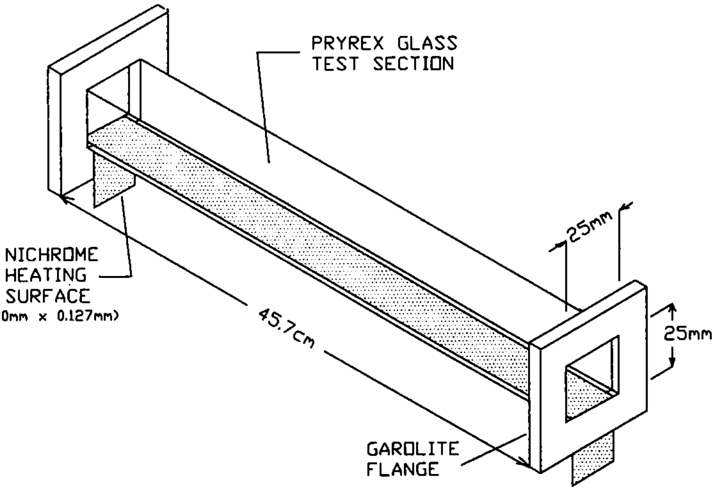

FIG. 2. Isometric view of transparent test section.

FIG. 3. Photograph of vapor bubble departure and lift-off at $G = 207$ kg m^{-2} s^{-1} and $q_w = 18.9$ kW m^{-2}; flow direction is from left to right.

across the two brass blocks with 2 gauge cable. The voltage and current into the strip were measured with a Fluke digital multimeter with an uncertainty less than ±1%.

Viatran model 2416 static pressure transducers have been installed at the inlet and outlet of the test section to measure the saturation pressure. They have an accuracy of ±0.5% of full scale (30 psig). All bulk temperature and exterior temperature measurements are made with type E thermocouples, which are accurate to within ±0.5°C and repeatable to within ±0.1°C. All analog signals have been inputed to an Access 12 bit digital data acquisition system that consists of two 16 channel multiplexer cards with programmable gain from 1 to 1000. The multiplexer cards were interfaced with an 8 channel, 12 bit analog to digital (A/D) converter which was mounted in an AT style personal computer. A scanning rate of 500 Hz was typically used.

All optical measurements for vapor bubble departure in this work have been accomplished with a digital imaging facility. The facility consists of a Videk Megaplus CCD camera with 1320 × 1035 pixel resolution. The CCD camera is equipped with a Vivitar 50 mm macro lens with high resolution and low optical distortion. The output of the CCD camera was inputed to an Epix 4 megabyte framegrabber. The framegrabber allows for either high resolution (1320 × 1035) or low resolution (640 × 480) imaging. In addition, the framegrabber controls the timing sequence for a Sunpak 622 flash system. The image is then displayed on a Sony analog monitor with a resolution of 1000 lines per inch. The length of the longest chord parallel to the heating surface which bisects the vapor bubble is taken to be the characteristic bubble diameter.

Measurements for vapor bubble departure diameter, contact angles, and surface/bubble contact diameter were made off the Sony monitor. The uncertainty of the departure diameter is ±0.03 mm and that of the contact angles is ±10°. A typical flash photograph showing vapor bubble departure and lift-off for mass flux $G = 207$ kg m^{-2} s^{-1}, and heat flux, $q_w = 18.9$ kW m^{-2}, is shown in Fig. 3. In every photograph there were bubbles away from the heating surface but within the depth of field. Their point of origin could not be precisely determined. Therefore, only vapor bubbles in which a sequence of at least three images emerge from a known nucleation site, as

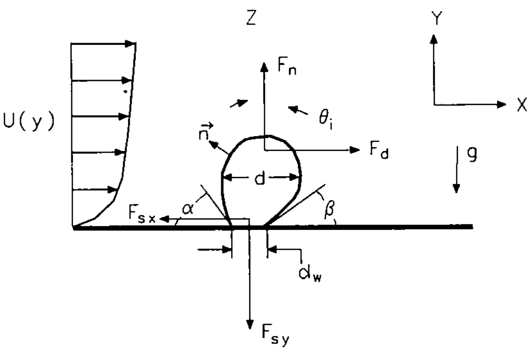

FIG. 4. Schematic diagram of growing vapor bubble attached to a heating surface in shear flow.

shown in Fig. 3, were used to determine the departure diameter. Figure 4 is a schematic representation of a growing vapor bubble attached to a heating surface in the presence of shear flow. Due to the inherent instability of two-phase flow systems, large slugs of liquid periodically passed through the test section. Photographs were discarded if a slug was present.

3. EXPERIMENTAL RESULTS

In order to gain insight into which forces are important in controlling vapor bubble departure, probability density functions (pdfs) for the departure diameter have been obtained over a range of flow conditions. Typically, a total of 200 bubble diameter measurements were used to construct a pdf for the departure diameter. In Fig. 5(a), pdfs, represented by the number of bubbles normalized (n/N), are shown for a constant heat flux, $q_w = 17.6$ kW m^{-2} and four different mass fluxes, $G = 133$, 181, 236, and 285 kg m^{-2} s^{-1}. Figures 5(b) and (c) show the pdfs for higher heat fluxes, $q_w = 20.2$ and 22.0 kW m^{-2}, respectively, at three different mass fluxes. For all of the measurements obtained, the two-phase flow regime was stratified and the boiling regime was that of isolated bubbles. From Figs. 5(a)–(c), it can be seen that the mean departure diameter decreases with increasing mass flux, which highlights the influence of the quasi-steady drag. However, the standard deviation of departure diameter from the mean is not much different than the mean value. This clearly suggests that the vapor bubble departure process is stochastic in nature. The most likely origin of the randomness in d is due to turbulent fluctuations which are characteristic of two-phase flow as well as spatial and temporal variations of wall superheat along the heating surface. The influence of turbulence on the departure diameter pdfs is currently under investigation. Although the pdfs shown in Figs. 5(a)–(c) behave in much the same manner, increasing the heat flux appears to shift the pdfs toward larger diameters. The dependence of the pdfs on heat flux will be discussed in further detail shortly. Because visualization of the nucleation sites is required to measure the departure diameter, the pdf data acquired herein are limited to specific ranges of heat and mass flux combinations. If the heat flux is too high at a given mass flux, the nucleation site density becomes too large and it is difficult to visually distinguish individual nucleation sites. If the heat flux is too low, the nucleation sites will be suppressed.

Figures 6(a)–(d) show the effect of heat flux on the vapor bubble departure diameter pdfs at $G = 136$, 183, 234, and 285 kg m^{-2} s^{-1}, respectively. In general, increasing the heat flux has a tendency to increase the mean departure diameter. However, the degree to which the heat flux influences the mean departure diameter strongly depends on flow conditions. At low mass flux, as shown in Figs. 6(a) and (b), increasing the heat flux tends to increase the departure diameter. However, at higher mass flux, as shown in Figs. 6(a)

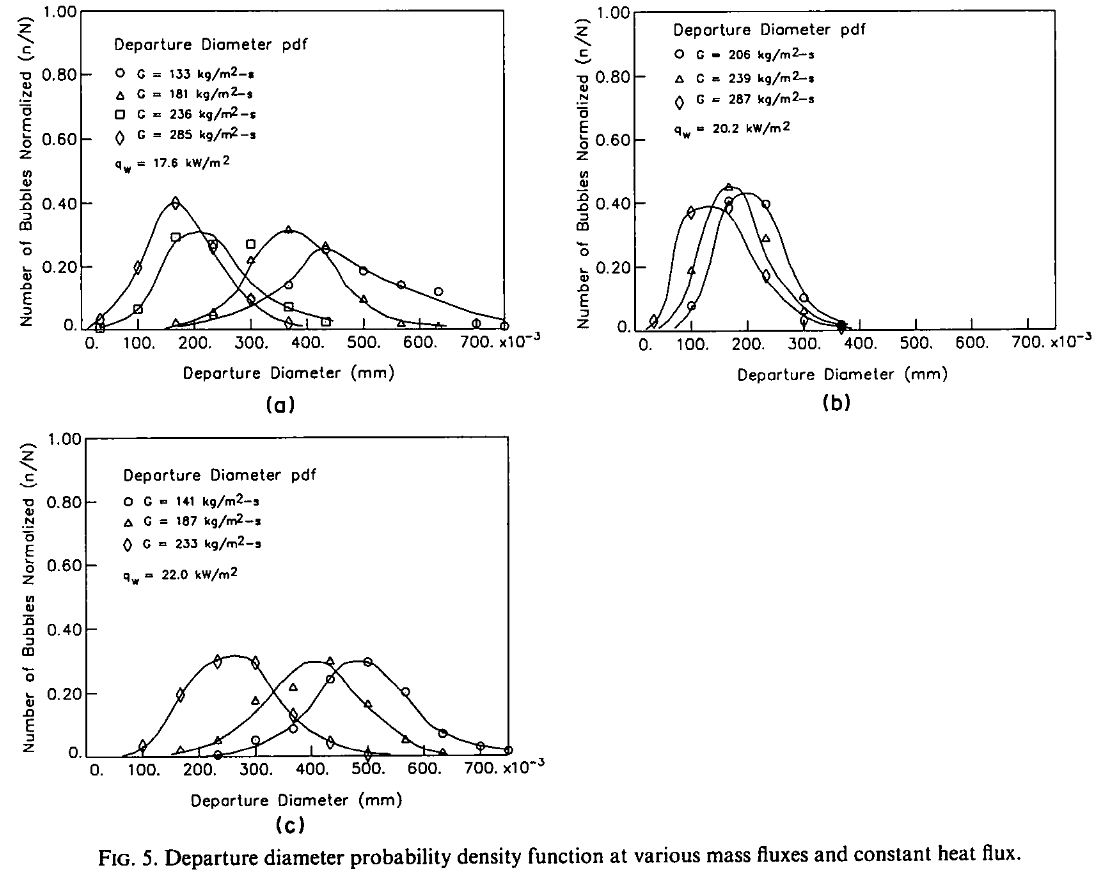

(a) (b) (c)

FIG. 5. Departure diameter probability density function at various mass fluxes and constant heat flux.

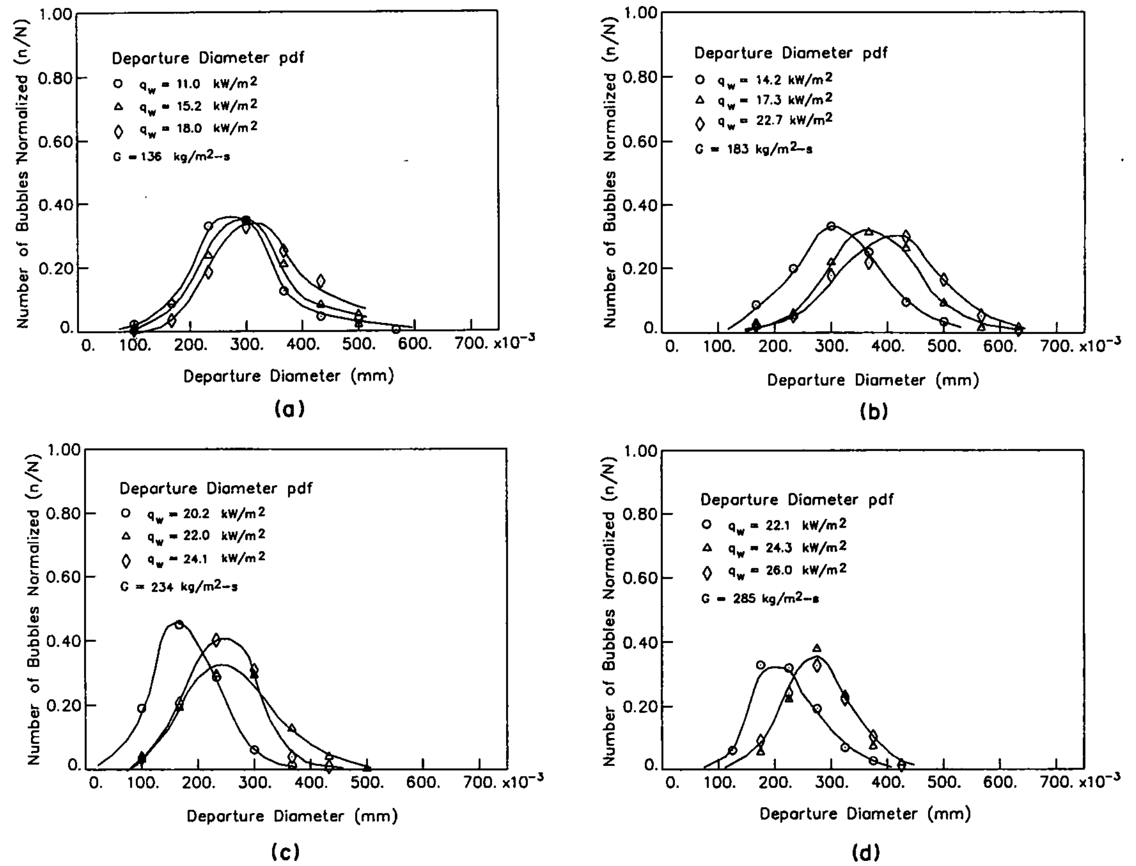

FIG. 6. Departure diameter probability density function at various heat fluxes and constant mass flux.

and (d), increasing the heat flux beyond a threshold does not appear to significantly influence the departure diameter. In order to understand the effect of the heat flux on the departure diameter, it is necessary to consider the fact that in flow boiling while vapor bubbles remain attached to a nucleation site they are typically inclined at an angle θ_i as shown in Fig. 4. Thus, as the vapor bubble grows it induces a force in the direction opposite to the fluid motion. At otherwise similar flow conditions, increasing the heat flux will increase the vapor bubble growth rate due to increased wall superheat, ΔT_{sat}. The unsteady force due to asymmetrical bubble growth will be enhanced, which increases the departure diameter. Further insight into the influence of the quasi-steady drag and drag due to asymmetrical bubble growth on the departure diameter will be gained from the analysis which follows.

4. ANALYSIS

To understand the influence of flow conditions on bubble departure, various forces acting on a bubble, as shown in Fig. 4, in the directions parallel and normal to a horizontal heating surface are analyzed. The forces acting on the bubble in the x- and y-directions are

$$\Sigma F_x = F_{sx} + F_{qs} + F_{dux} \tag{1}$$

$$\Sigma F_y = F_{sy} + F_{duy} + F_{sL} + F_b + F_h + F_{cp} \tag{2}$$

where F_s is the surface tension force, F_{qs} the quasi-steady drag in the flow direction, F_{du} the unsteady drag due to asymmetrical growth of the bubble and the dynamic effect of the unsteady liquid flow such as the history force and the added mass force, F_{sL} the shear lift force, F_b the buoyancy force, F_h the force due to the hydrodynamic pressure, and F_{cp} the contact pressure force accounting for the fact that the bubble is in contact with a solid wall rather than being completely surrounded by liquid. All of the forces appearing in equations (1) and (2) will be discussed and explained in detail. In the following analysis leading to the prediction of the mean departure diameter, the dynamic effects of turbulence and wave motion will be ignored and the justification for doing so will be given in Section 4.2. In estimating the various forces, a typical bubble will be considered. The following parameters have been measured: $\bar{d} = 0.26$ mm, $d_w \sim 0.09$ mm, $\alpha \sim \pi/4$, $\beta \sim \pi/5$, at $G = 223$ kg m^{-2} s^{-1}, $\delta = 6.5$ mm, $X = 0.106$, $u_l = 0.52$ m s^{-1}, $q_w = 23.6$ kW m^{-2}, $T_{sat} = 60$°C and $\Delta T_{sat} = 15.8$°C, where $\bar{d}$ is the mean departure diameter, d_w the surface/bubble contact diameter, α and β the respective advancing and receding contact angles on the x–y plane, δ the mean liquid film thickness, X the mean vapor quality, u_l the mean liquid velocity, q_w the wall heat flux, T_{sat} the saturation temperature, and ΔT_{sat}

the mean wall superheat. For the above condition the R113 fluid properties are as follows, $\sigma = 0.0135$ N m^{-1}, $\rho_l = 1479$ kg m^{-3}, $\rho_v = 10.7$ kg m^{-3}, and $\nu_l = 2.91 \times 10^{-7}$ m^2 s^{-1}, where σ is the surface tension coefficient, ρ_l and ρ_v the liquid and vapor densities, respectively, and ν_l the liquid kinematic viscosity. Due to measurement error near the base of the bubble, reliable determination of d_w was not possible. The value reported for d_w is probably the maximum it can be, although it is possible that it is significantly smaller.

4.1. *Surface tension force*

In order to determine F_{sx} and F_{sy}, it is necessary to differentiate the advancing contact angle, α, from the receding contact angle, β, on the plane parallel to the flow direction and normal to the heating surface as shown in Fig. 4. A third order polynomial is assumed for the general contact angle, γ

$$\gamma(\phi) = \beta + (\alpha - \beta)\left[3\left(\frac{\phi}{\pi}\right)^2 - 2\left(\frac{\phi}{\pi}\right)^3\right], \quad 0 \leqslant \phi \leqslant \pi \tag{3}$$

where ϕ is the polar angle around the bubble. It satisfies $\gamma(0) = \beta$ and $\gamma(\pi) = \alpha$ and the symmetry conditions $\gamma'(0) = \gamma'(\pi) = 0$. This is a good representation when the difference in α and β is not large. The respective surface tension forces in the x- and y-direction are given by

$$F_{sx} = -\int_0^\pi d_w \sigma \cos\gamma \cos\phi \, d\phi \tag{4a}$$

$$F_{sy} = -\int_0^\pi d_w \sigma \sin\gamma \, d\phi. \tag{4b}$$

For the purpose of evaluating (4a) and (4b) and obtaining a closed form approximation for F_{sx} and F_{sy}, equation (3) is further simplified to

$$\gamma(\phi) \sim \beta + (\alpha - \beta)\frac{\phi}{\pi}, \quad 0 \leqslant \phi \leqslant \pi. \tag{5}$$

Substitution of (5) into (4a) and (4b) yields

$$F_{sx} \sim -d_w \sigma \frac{\pi(\alpha - \beta)}{\pi^2 - (\alpha - \beta)^2}[\sin\alpha + \sin\beta] \tag{6a}$$

$$F_{sy} \sim -d_w \sigma \frac{\pi}{\alpha - \beta}[\cos\beta - \cos\alpha]. \tag{6b}$$

Results of numerical integration of (4a) and (4b) using (3) indicate that F_{sx} given by (6a) should be corrected by multiplying by a factor of 1.25 and F_{sy} given by (6b) does not require correction. In the limit as $\alpha \to \beta$, $F_{sx} \to -2.5 d_w \sigma(\alpha - \beta)(\sin\alpha)/\pi$ and $F_{sy} \to -d_w \sigma \pi \sin\alpha$. For the typical bubble considered here, $F_{sx} = -9.9 \times 10^{-8}$ N and $F_{sy} = -2.5 \times 10^{-6}$ N, with $F_{sx}/F_{sy} \sim 0.04$.

4.2. *Quasi-steady drag*

For a time varying uniform viscous flow over a stationary bubble, the unsteady drag consists of a quasi-steady component, a memory or history term, and an added-mass component [7]. For the typical flow conditions cited previously, the turbulence velocity in the wall region is scaled by u^*, the friction velocity. Based on estimates for single-phase flow [8], $u^* \sim 0.04 u_l \sim 0.02$ m s^{-1}. The most energetic eddy is associated with a double roller-eddy with a spanwise spacing of $\lambda_z^+ = \lambda_z u^*/\nu \sim 100$. Thus a typical time scale for the energetic eddy in the wall region is $t_{turb} \sim \lambda/u^* = 100\nu/(u^*)^2 \sim 7 \times 10^{-2}$ s. If λ_x, the integral length scale in the streamwise direction, was used t_{turb} would be greater by a factor of 2–3 [9]. The unsteadiness due to the interfacial waves is associated with a time scale on the order of 10^{-1} s [6]. On the other hand, the bubble growth and departure time scale, t_{growth}, is at most 10^{-3} s. The Stokes number, which is a measure of the relative importance of the unsteady force compared to the quasi-steady drag, based on t_{turb} is $\varepsilon_{turb} = [a^2/(\nu t_{turb})]^{1/2} \sim 0.91$ while $\varepsilon_{growth} = [a^2/(\nu t_{growth})]^{1/2} \sim 7.6$. The implication here is that the unsteady force due to bubble growth is dominant. The history and added-mass forces oscillate in time with their respective amplitudes scaled by u^*. Their contribution to the departure diameter is thus insignificant. Hereafter, the unsteady drag F_{du} will exclusively denote the force due to the bubble growth. Its effect on bubble dynamics is accounted for phenomenologically as described in Section 4.3.

There does not at present exist an expression for the quasi-steady drag for a non-spherical bubble in the presence of a wall. Mei and Klausner [7] obtained an expression for the steady drag for an unbounded uniform flow over a spherical bubble for $0 \leqslant Re \leqslant 1000$ and is given by

$$\frac{F_{steady}}{6\pi\rho_l \nu U a} = \frac{2}{3} + \left[\left(\frac{12}{Re}\right)^n + 0.796^n\right]^{-1/n} \tag{7}$$

where U is the uniform flow velocity, $a = d/2$ the bubble radius, $Re = 2Ua/\nu$ the Reynolds number, and $n = 0.65$. In the present analysis F_{qs} is evaluated from equation (7) by taking a to be the instantaneous bubble radius and U to be the fluid velocity at the center of the bubble. Although the forces on a growing bubble are governed by the instantaneous turbulent velocity field, when evaluating the *mean* departure diameter, the time-averaged velocity profile can be used. The time-averaged velocity near the wall is assumed to follow the turbulent single-phase flow relation proposed by Reichardt and is given by Hinze [8] as

$$\frac{U(y)}{u^*} = \frac{1}{\kappa}\ln\left(1 + \kappa\frac{yu^*}{\nu}\right) + c\left[1 - \exp\left(-\frac{\frac{yu^*}{\nu}}{\chi}\right) - \frac{\frac{yu^*}{\nu}}{\chi}\exp\left(-0.33\frac{yu^*}{\nu}\right)\right] \tag{8}$$

where $\kappa = 0.4$, $\chi = 11$, and $c = 7.4$. In the present analysis u^*/u_l is assumed to be 0.04 where u_l is the mean liquid velocity for two-phase flow. It is related to the mass flux G, vapor quality X, and liquid film thickness, δ, through

$$u_l = \frac{G(1-X)D}{\rho_l \delta} \tag{9}$$

where D is the inner width of the square channel. For the typical bubble F_{qs} is estimated to be 2.8×10^{-7} N. It is seen that F_{qs} is greater than F_{sx} by a factor of 2.8, which implies that there must be another force acting on the vapor bubble in the negative x-direction which can balance the quasi-steady drag prior to bubble departure. This force is due to asymmetrical bubble growth.

4.3. *Force due to asymmetrical bubble growth*

Here two ideal cases for bubble growth are considered: (1) a uniform unbounded inviscid liquid over an expanding spherical bubble, and (2) a hemispherical bubble attached to a wall and expanding in a stagnant liquid. For the first case it can be shown by solving the velocity potential and applying the Bernoulli equation that the drag due to bubble growth is

$$\vec{\mathbf{F}}_1 = \tfrac{3}{2} m_l U \frac{\dot{a}}{a} \vec{\mathbf{e}}_x \tag{10}$$

where $m_l = 4/3\pi\rho_l a^3$ is the mass of liquid displaced by the bubble, $(\vec{\ })$ denotes a vector quantity, $\vec{\mathbf{e}}_x$ is the unit vector in the x-direction, and $(\dot{\ })$ denotes differentiation with respect to time. This force accounts for the inviscid interaction between the uniform flow and the flow induced by the expansion of the bubble. It is sensitive to the bubble shape. For the second case, the pressure distribution over an expanding bubble is

$$P = P_\infty + \rho_l[a\ddot{a} + \tfrac{3}{2}\dot{a}^2]. \tag{11}$$

The force on the hemispherical bubble due to the growth is thus

$$\vec{\mathbf{F}}_2 = -\rho_l \pi a^2 [a\ddot{a} + \tfrac{3}{2}\dot{a}^2] \vec{\mathbf{e}}_y. \tag{12}$$

The contribution from P_∞ is lumped into a reference pressure when evaluating the contact pressure force as is shown in Section 4.5.

During the actual bubble growth process, the bubble is distorted and inclined in the flow direction due to the quasi-steady drag and possibly F_{1x} during the initial stages of growth. This asymmetry during the bubble growth has two consequences. First, it will reduce F_{1x} by reducing the pressure near the region facing the flow. Secondly, it induces an x-component of $\vec{\mathbf{F}}_2$ in the direction opposite the mean flow, which may be approximated as

$$F_{2x} \sim -\rho_l \pi a^2 (a\ddot{a} + \tfrac{3}{2}\dot{a}^2) \sin\theta_i \tag{13}$$

where θ_i is the inclination angle measured from the y-axis. The experimental measurements presented earlier indicate that an increase in the heat flux at a given mass flux, which leads to a faster bubble growth rate, results in an increase in $\bar{d}$. This experimental finding suggests that the effect of bubble growth is to provide a net x-component force in the direction opposite to the flow. Furthermore, the preceding analysis has demonstrated that the surface tension force is insufficient to balance the quasi-steady drag. Consequently, the net force due to asymmetrical growth must act in the negative x-direction. Based on these considerations, equation (13) is used to model the x-component force due to asymmetrical growth, with $F_{\mathrm{du}x} \sim F_{2x}$. It is not currently possible to predict the inclination angle, θ_i, analytically. Thus θ_i is treated here as an empirical constant to be determined experimentally.

To predict the time rate of change of the radius for a spherical growing vapor bubble at a wall, the expression developed by Mikic *et al.* [10] is used here:

$$a(t) = \frac{2}{3}\frac{B^2}{A}[(t^+ + 1)^{3/2} - (t^+)^{3/2} - 1] \tag{14}$$

$$t^+ = \frac{A^2 t}{B^2} \tag{15}$$

where A and B are related to the wall superheat, ΔT_{sat}, and are given by

$$A = \left[\frac{\pi}{7}\frac{h_{fg}\rho_v \Delta T_{\mathrm{sat}}}{\rho_l T_{\mathrm{sat}}}\right]^{1/2} \tag{16}$$

$$B = \left[\frac{12}{\pi}\eta_l\right]^{1/2} \frac{\Delta T_{\mathrm{sat}} c_{pl} \rho_l}{h_{fg}\rho_v} \tag{17}$$

where η_l is the liquid thermal diffusivity and c_{pl} the liquid specific heat. Taking $\theta_i \sim \pi/18$, which is based on the average of 35 data points at different flow conditions, it is found that $F_{\mathrm{du}x} \sim -1.8 \times 10^{-7}$ N for the typical bubble at the time when $a(t)$ equals the measured departure radius. It is seen that $\Sigma F_x = F_{qs} + F_{\mathrm{du}x} + F_{sx} = 1.0 \times 10^{-9}$ N $\ll F_{qs} \sim 2.8 \times 10^{-7}$ N at the point of departure for the typical bubble. It would seem that the assumptions used to estimate these forces are quite reasonable. Subsequent to the point of departure $F_{qs} + F_{\mathrm{du}x} + F_{sx} > 0$ and thus the bubble will begin to slide along the heating surface until it lifts off.

The unsteady force due to asymmetrical growth which acts in the negative y-direction, $F_{\mathrm{du}y}$, may also be estimated from equation (13) if $\cos\theta_i$ is substituted for $\sin\theta_i$. For the typical bubble $F_{\mathrm{du}y} \sim -1.0 \times 10^{-6}$ N.

4.4. *Shear lift force*

Mei and Klausner [11] recently derived an expression for the shear lift force on a spherical bubble in an unbounded flow field at low Reynolds number. The shear lift force is two-thirds of that for a solid sphere derived by Saffman [12, 13]. Combined with the result of Auton [14] for the shear lift force on a bubble in the inviscid flow limit with small shear rate, an interpolation was developed for the purpose of estimating the shear lift force over a large range of Reynolds number and is given as

$$C_{\mathrm{L}} = \frac{F_{\mathrm{sL}}}{\frac{1}{2}\rho_{\mathrm{l}} U^2 \pi a^2} = 3.877 G_{\mathrm{s}}^{1/2} \times [Re^{-m/2} + (0.344 G_{\mathrm{s}}^{1/2})^m]^{1/m}, \quad m = 4 \tag{18}$$

where

$$G_{\mathrm{s}} = \left|\frac{\mathrm{d}U}{\mathrm{d}y}\right| \frac{a}{U} \tag{19}$$

is the dimensionless shear rate of the oncoming flow. At present there is no expression available for the shear lift force on a bubble attached to a wall. Equation (18) is used to estimate the shear lift force for the present analysis. For the typical bubble, $F_{\mathrm{sL}} \sim 1.3 \times 10^{-6}$ N using Reichardt's mean velocity profile for U and G_{s} at $y = a$ as was explained in Section 4.2.

4.5. *Buoyancy, hydrodynamic, and contact pressure forces*

Consider a bubble attached to the wall with S_1 and S_2 denoting the bubble surfaces in contact with the liquid and the wall, respectively. Let P_{v} be the vapor pressure inside the bubble and $P = \Gamma - \rho_{\mathrm{l}} g y$ be the total pressure on the outside surface, in which Γ is the hydrodynamic pressure due to fluid flow and $-\rho_{\mathrm{l}} g y$ is the hydrostatic pressure. The viscous and dynamic effects due to growth have been accounted for separately in the consideration of the quasi-steady drag, shear lift force, and the force due to bubble growth. The total pressure force on the bubble in the y-direction is

$$\begin{aligned} F_{\mathrm{p}y} &= -\int_{s_1} P n_y \,\mathrm{d}A + \int_{s_1} P_{\mathrm{v}} n_y \,\mathrm{d}A \\ &= -\int_{s_1} (\Gamma - \rho_{\mathrm{l}} g y) n_y \,\mathrm{d}A + \int_{s_1+s_2} P_{\mathrm{v}} n_y \,\mathrm{d}A \\ &\quad - \int_{s_2} P_{\mathrm{v}} n_y \,\mathrm{d}A = -\int_{s_1} (\Gamma - \Gamma_{\mathrm{r}}) n_y \,\mathrm{d}A \\ &\quad - \int_{s_1+s_2} (\Gamma_{\mathrm{r}} - \rho_{\mathrm{l}} g y - P_{\mathrm{v}}) n_y \,\mathrm{d}A \\ &\quad + \int_{s_2} (\Gamma_{\mathrm{r}} - \rho_{\mathrm{l}} g y - P_{\mathrm{v}}) n_y \,\mathrm{d}A \end{aligned} \tag{20}$$

where $\vec{n}$ is the outward normal of the bubble surface, n_y is its y-component, and Γ_{r} is a reference pressure at $y = 0$. The above can be further simplified to

$$F_{\mathrm{p}y} = F_{\mathrm{b}} + F_{\mathrm{h}} + F_{\mathrm{cp}} \tag{21}$$

where

$$\begin{aligned} F_{\mathrm{b}} &= -\int_{s_1+s_2} (\Gamma_{\mathrm{r}} - \rho_{\mathrm{l}} g y - P_{\mathrm{v}}) n_y \,\mathrm{d}A \\ &= \tfrac{4}{3}\pi a^3 (\rho_{\mathrm{l}} - \rho_{\mathrm{v}}) g \end{aligned} \tag{22}$$

is the buoyancy force, and

$$F_{\mathrm{h}} = -\int_{s_1} (\Gamma - \Gamma_{\mathrm{r}}) n_y \,\mathrm{d}A \tag{23}$$

is the force due to the hydrodynamic pressure (relative to the reference pressure, Γ_{r}). This pressure $(\Gamma - \Gamma_{\mathrm{r}})$ may be evaluated from the Bernoulli equation if the surface velocity on the bubble is known. The remaining force component F_{cp} in equation (21) is here identified as the contact pressure force

$$\begin{aligned} F_{\mathrm{cp}} &= \int_{s_2} (\Gamma_{\mathrm{r}} - \rho_{\mathrm{l}} g y - P_{\mathrm{v}}) n_y \,\mathrm{d}A \\ &= -(\Gamma_{\mathrm{r}} - \rho_{\mathrm{l}} g y - P_{\mathrm{v}})|_{y=0} A_2 = \frac{\pi d_{\mathrm{w}}^2}{4} \frac{2\sigma}{r_{\mathrm{r}}} \end{aligned} \tag{24}$$

where r_{r} is the radius of curvature of the bubble at the reference point on the surface $y = 0$, and is typically an order of magnitude greater than the mean bubble radius. This contact pressure force is due to the pressure difference inside and outside of the bubble at the reference point over the contact area. The reference point is immaterial because Γ_{r} also appears in equation (23). Assuming that $r_{\mathrm{r}} \sim 5a$, then $F_{\mathrm{cp}} \sim 1.7 \times 10^{-7}$ N, which is much less than $F_{\mathrm{s}y}$. The buoyancy force for the typical bubble is $F_{\mathrm{b}} \sim 1.0 \times 10^{-7}$ N. The hydrodynamic force, F_{h}, may be estimated by considering an inviscid flow over a sphere in an unbounded flow field. Due to the symmetry over the majority of the bubble surface, the contribution to F_{h} is from the pressure on the top of the bubble over an area $\pi d_{\mathrm{w}}^2/4$ and is on the order of

$$F_{\mathrm{h}} \sim \frac{1}{2}\frac{9}{4}\rho_{\mathrm{l}} U^2 \frac{\pi d_{\mathrm{w}}^2}{4}. \tag{25}$$

Again U is evaluated at $y = a$. For the typical bubble, $F_{\mathrm{h}} \sim 2.7 \times 10^{-7}$ N.

4.6. *Prediction for the departure diameter*

While a vapor bubble remains attached to its nucleation site, the following conditions must be satisfied: (i) $\Sigma F_x = 0$ and (ii) $\Sigma F_y = 0$. Should condition (i) be violated prior to condition (ii) the bubble will slide along the heating surface before lifting off, as was observed for the majority of experiments. In this circumstance the point at which ΣF_x is just greater than zero is the criterion for departure. However, should condition (ii) be violated prior to condition (i), the bubble will lift off the surface directly without first sliding, and the point at which ΣF_y is just greater than zero is the criterion for both departure and lift-off. Therefore, a prerequisite to predicting the departure diameter is to determine whether it is condition (i) or condition (ii) that is violated first.

Although $\Sigma F_x = 0$ and $\Sigma F_y = 0$ while the bubble remains attached to the nucleation site, the above analysis will predict that $\Sigma F_x < 0$ and $\Sigma F_y < 0$ until the point of departure. The reason is that the contact angles as well as the inclination angle in reality evolve from the point of inception until the point of departure. Because the evolution process of these angles is unknown, they are taken to be constant in the prediction of the mean departure diameter.

To recapitulate, the forces on the typical bubble in the x-direction are $F_{sx} \sim -9.9\times10^{-8}$ N, $F_{qs} \sim 2.8\times10^{-7}$ N, and $F_{dux} \sim -1.8\times10^{-7}$ N and those in the y-direction are $F_{sy} \sim -2.5\times10^{-6}$ N, $F_{duy} \sim -1.0\times10^{-6}$ N, $F_{sL} \sim 1.3\times10^{-6}$ N, $F_b \sim 1.0\times10^{-7}$ N, $F_{cp} \sim 1.7\times10^{-7}$ N, and $F_h \sim 2.7\times10^{-7}$ N; $\Sigma F_x \sim 1.0\times10^{-9}$ N and $\Sigma F_y \sim -1.7\times10^{-6}$ N. This result indicates that the vapor bubble will slide before lifting-off. Using the above criteria, the predicted departure diameter is $\bar{d} = 0.25$ mm. The prediction here is quite good considering that the measured departure diameter is $\bar{d} = 0.26$ mm. The foregoing force balance analysis can also be used to predict the mean bubble diameter at the point of vapor bubble lift-off. Experimental investigations examining the dependence of the lift-off diameter on u_l and ΔT_{sat} are currently in progress and the results will be forthcoming in a subsequent work.

5. ANALYTICAL RESULTS AND DISCUSSION

In order to assess the validity of the bubble departure analysis, 35 sets of data for the mean departure diameter given in Table 1 are compared against the predicted values. Accurate measurements of α, β, and d_w were very difficult due to the lack of resolution at the base of the bubble. Of these, d_w was the most difficult to accurately measure. While it is possible that the contact area approaches zero near departure and lift-off, the value reported for the typical bubble is possibly its maximum. The uncertainty in the measurement of α and β was about $\pm 10°$. It was found that these parameters were quite scattered around a mean, but the difference in the mean among various data sets was within the range of uncertainty of the measurements. Therefore, the values of α and β were taken to be the same as those reported for the typical bubble. Taking d_w to be its possible maximum, the value of θ_i which gave the best fit to the data is $\pi/18$. As can be seen from the photograph in Fig. 3, this is quite reasonable. Figure 7 compares the predicted values with the measured values of departure diameter for the 35 data points. Considering the complexity of bubble departure, the difficulty in obtaining the measurements, and various approximations used to develop the departure analysis, the agreement is quite satisfactory.

Table 1. Mean vapor bubble departure diameter at various flow conditions

G (kg m^{-2}s^{-1})	x_{inlet}	T_{sat} (°C)	δ (mm)	$\bar{d}$ (mm)	q_w (kW m^{-2})	ΔT_{sat} (°C)
113	0.093	59.8	4.6	0.36	17.7	16.4
115	0.165	60.7	5.5	0.46	17.4	15.1
132	0.008	71.9	7.9	0.31	17.4	12.0
133	0.069	57.7	6.9	0.46	17.5	16.9
135	0.092	65.9	4.3	0.36	17.6	14.3
137	0.123	60.8	5.3	0.36	14.9	14.5
140	0.077	55.8	6.4	0.28	11.0	12.7
157	0.038	58.5	7.3	0.42	17.7	16.3
175	0.094	61.6	5.9	0.31	17.4	14.1
180	0.002	69.9	7.3	0.27	17.6	12.3
181	0.076	58.1	8.7	0.37	17.3	16.6
181	0.071	58.2	8.6	0.31	14.2	14.4
188	0.132	57.8	6.1	0.40	22.7	17.0
189	0.050	57.7	7.6	0.41	18.1	15.9
189	0.092	60.9	5.2	0.30	14.8	13.6
196	0.039	61.9	7.9	0.29	17.9	13.9
200	0.112	57.9	6.8	0.30	22.3	16.8
204	0.057	59.1	6.5	0.30	17.9	15.3
206	0.055	56.8	6.0	0.21	20.2	17.3
214	0.084	62.6	5.2	0.21	17.3	12.9
223	0.100	60.0	6.5	0.26	23.6	15.8
233	0.082	57.2	7.1	0.24	24.1	17.4
233	0.073	59.6	8.1	0.28	19.6	15.5
233	0.090	59.4	5.8	0.26	23.6	15.1
234	0.071	61.7	6.4	0.28	15.2	13.4
234	0.081	57.1	7.5	0.26	21.1	16.6
236	0.047	60.5	7.7	0.24	17.9	14.0
239	0.062	57.5	5.95	0.18	20.2	16.1
249	0.059	59.2	8.2	0.25	17.8	13.8
265	0.068	63.5	6.0	0.18	17.4	12.1
285	0.076	56.2	5.2	0.28	26.0	17.7
285	0.072	56.3	5.6	0.28	24.3	17.6
285	0.059	61.5	8.1	0.18	17.9	11.9
285	0.070	56.4	5.6	0.22	22.1	15.4
287	0.061	58.8	6.1	0.16	20.2	13.6

In order to gain insight into the dependence of the departure diameter on the flow conditions, the influence of the mean liquid velocity and wall superheat on $\bar{d}$ have been investigated. Figure 8 shows the predicted departure diameter as a function of mean liquid velocity, u_l, ranging from 0 to 1.00 m s^{-1}, at three different wall superheats, ΔT_{sat} = 15, 18, and 21°C. Results are shown for the case where d_w = 0.09 mm. Two distinct regimes may be identified: (1) pool boiling regime at low velocity where bubbles depart the nucleation sites by lifting off the heating surface with-

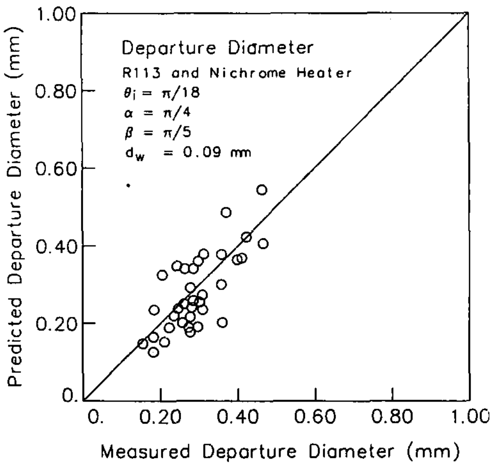

FIG. 7. Comparison of measured versus predicted departure diameter.

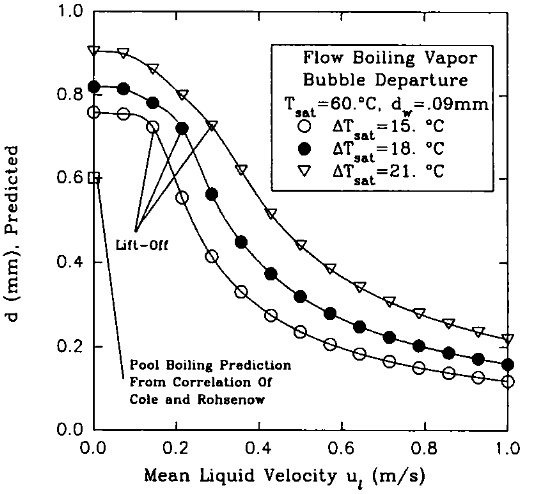

FIG. 8. Predicted departure diameter for $d_w = 0.09$ mm and u_l ranging from 0 to 1.0 m s^{-1} at $\Delta T_{sat} = 15$, 18, and 21°C.

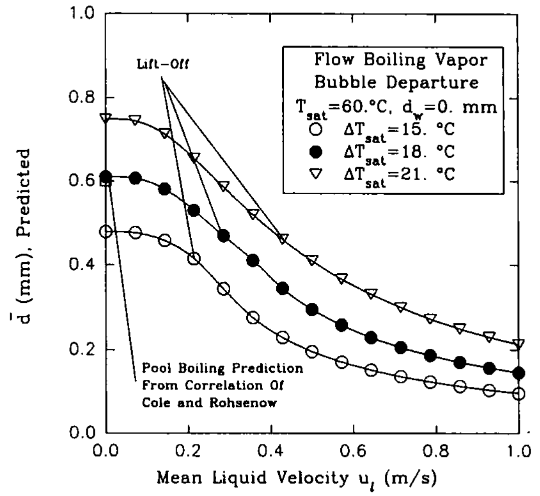

FIG. 9. Predicted departure diameter for $d_w = 0.0$ mm and u_l ranging from 0 to 1.0 m s^{-1} at $\Delta T_{sat} = 15$, 18, and 21°C.

out first sliding; (2) flow boiling regime where vapor bubbles depart the nucleation sites by sliding along the heating surface. In the pool boiling regime, $\bar{d}$ is mainly controlled by ΔT_{sat} and is insensitive to u_l. Also shown in Fig. 8 is the predicted departure diameter using the pool boiling correlation of Cole and Rohsenow [15]. It is clear that pool boiling correlations for departure diameter are not applicable to flow boiling because u_l is not accounted for. As u_l increases, the lift-off diameter decreases slightly in the pool boiling regime due to an increasing shear lift force. As ΔT_{sat} increases the pool boiling regime expands towards larger u_l.

In the flow boiling regime, Fig. 8 shows that $\bar{d}$ decreases rapidly with increasing u_l and follows a power law relationship with $\bar{d} \sim 1/u_l$. This relation implies that an incremental change in u_l results in a significant change in departure diameter at low velocity and an insignificant change at high velocity. In the flow boiling experiments, both q_w and G are increased (or decreased) to accommodate the visualization and measurement. It has been observed that as q_w and G increase, there are insignificant changes in $\bar{d}$. However, this does not imply that $\bar{d}$ does not depend on q_w and G. When u_l increases, which can be achieved by increasing G, from 0.35 to 0.50 and 0.80 m s^{-1}, and ΔT_{sat} changes from 15 to 18, and 21°C, which can be achieved by increasing q_w, $\bar{d}$ remains at about 0.25 mm because the increase in ΔT_{sat} negates the effect of increasing u_l.

In the preceding discussion, the contact diameter $d_w = 0.09$ mm was assumed throughout. It is possible from a physical standpoint that $d_w \to 0$ at the point of departure. This is probably the case for bubbles lifting off the heating surface due to the necking phenomenon, but whether or not this is the case for bubble departure is not quite clear. In the limiting case when d_w is taken to be zero, the inclination angle θ_i which gives the best fit to the data in Table 1 is $1.1\pi/18$. For this limiting case ($d_w = 0$ and $\theta_i = 1.1\pi/18$), the predicted departure diameters are shown in Fig. 9. Similar to Fig. 8, a pool boiling and flow boiling regime can be identified. At large u_l the predicted departure diameters are not much different from those in Fig. 8. However, in the pool boiling regime, there is considerable difference between the departure diameters shown in Fig. 9 compared with those in Fig. 8. Combining the prediction from Figs. 8 and 9 it may be postulated that the actual departure diameters lie between these limits. Nevertheless, based on the present theoretical framework, the $d_w = 0$ case is easier to use as a predictive tool because it is a universally valid lower limit.

6. CONCLUSIONS

(i) Vapor bubble departure diameters in forced convection boiling have been experimentally obtained over a range of mass flux, G, and heat flux, q_w, for the stratified two-phase flow regime.

(ii) For the flow conditions experimentally investigated, the overwhelming majority of the bubbles leave the nucleation sites by sliding a finite distance along the heating surface before lifting off the wall.

(iii) The measured departure diameter probability density functions demonstrate a systematic dependence on G and q_w. In general an increase in G shifts the pdf curve towards lower departure diameters, and an increase in q_w shifts the pdf curve toward larger diameters.

(iv) A detailed analysis of various forces acting on a growing vapor bubble attached to a wall is presented. It is found that the surface tension force alone cannot prevent the vapor bubble from departing. The resistance of the liquid on the bubble due to asymmetrical bubble growth acting in the direction opposite to the fluid motion is important in holding the bubble at the nucleation site before departure. This analysis also indicates that for the flow conditions experimentally investigated, the bubble will slide along the heating surface following departure and prior to lift-off.

(v) The above analysis is used as an analytical tool to predict the mean departure diameter, $\bar{d}$, of the bubble. Satisfactory agreement with the experimental measurements is obtained.

(vi) Based on the analytical prediction of the departure diameter, two important quantities which influence the mean departure diameter have been identified. They are the mean liquid velocity, u_l, and the mean wall superheat, ΔT_{sat}. An increase in u_l leads to a decrease in $\bar{d}$, while an increase in ΔT_{sat} leads to an increase in $\bar{d}$.

(vii) The analysis demonstrates that departure diameter results for pool boiling are not applicable to flow boiling. In fact, the departure mechanisms are quite different. This casts doubt on the validity of using pool boiling correlations to model the microconvective component of heat transfer in flow boiling.

Acknowledgements—This material is based on work supported by the National Science Foundation under Grant No. CTS-9008269.

REFERENCES

1. Y. P. Chang, Some possible critical conditions in nucleate boiling, *ASME J. Heat Transfer* **85**, 89–100 (1963).
2. Y. Y. Hsu and R. W. Graham, A visual study of two-phase flow in a vertical tube with heat addition, NASA TND-1564 (1963).
3. S. Levy, Forced convection subcooled boiling-prediction of vapor volumetric fraction, *Int. J. Heat Mass Transfer* **10**, 951–965 (1967).
4. N. Koumoutsos, R. Moissis and A. Spyridonos, A study of bubble departure in forced-convection boiling, *ASME J. Heat Transfer* **90**, 223–230 (1968).
5. M. G. Cooper, K. Mori and C. R. Stone, Behavior of vapor bubbles growing at a wall with forced flow, *Int. J. Heat Mass Transfer* **26**, 1489–1507 (1983).
6. J. F. Klausner, L. Z. Zeng and D. M. Bernhard, Development of a film thickness probe using capacitance for asymmetrical two phase flow with heat addition, *Rev. Scient. Instrum.* **63**, 3147–3152 (1992).
7. R. Mei and J. F. Klausner, Unsteady force on a spherical bubble at finite Reynolds number with small fluctuations in the free-stream velocity, *Physics Fluids* **4**, 63–70 (1992).
8. J. O. Hinze, *Turbulence*. McGraw-Hill, New York (1975).
9. S. L. Lyons, A direct simulation of turbulent channel flow with passive heat transfer, Ph.D. thesis, University of Illinois at Urbana–Champaign (1989).
10. B. B. Mikic, W. M. Rohsenow and P. Griffith, On bubble growth rates, *Int. J. Heat Mass Transfer* **13**, 657–666 (1970).
11. R. Mei and J. F. Klausner, Shear lift force on spherical bubbles (submitted for publication).
12. P. G. Saffman, The lift on a small sphere in a slow shear flow, *J. Fluid Mech.* **22**, 385–400 (1965).
13. P. G. Saffman, Corrigendum to 'The lift on a small sphere in a slow shear flow', *J. Fluid Mech.* **31**, 624 (1968).
14. T. R. Auton, The lift force on a spherical body in a rotational flow, *J. Fluid Mech.* **183**, 199–218 (1987).
15. R. Cole and W. M. Rohsenow, Correlation of bubble departure diameters for boiling of saturated liquids, *Chem. Engng Prog. Symp. Ser.* **65**, 211–213 (1969).